

# Correlated spectro-polarimetric study along the Z track in XTE J1701–462 puts constraints on its coronal geometry

Wei Yu<sup>1,2</sup>, Qingcui Bu<sup>4\*</sup>, Victor Doroshenko<sup>1</sup>, Lorenzo Ducci<sup>1,5</sup>, Long Ji<sup>6</sup>, Wenda Zhang<sup>7</sup>, Andrea Santangelo<sup>1</sup>, Shuangnan Zhang<sup>2,3</sup>, Anand Waghmare<sup>1</sup>, Mingyu Ge<sup>2</sup>, Yue Huang<sup>2</sup>, Hexin Liu<sup>2</sup>, Lian Tao<sup>2</sup>, Zixu Yang<sup>8</sup>, Liang Zhang<sup>2</sup>, and Jinlu Qu<sup>2,3</sup>

<sup>1</sup> Institut für Astronomie und Astrophysik, Kepler Center for Astro and Particle Physics, Eberhard Karls Universität, Sand 1, 72076 Tübingen, Germany

<sup>2</sup> Key Laboratory of Particle Astrophysics, Institute of High Energy Physics, Chinese Academy of Sciences, Beijing 100049, China

<sup>3</sup> University of Chinese Academy of Sciences, Chinese Academy of Sciences, Beijing 100049, China

<sup>4</sup> Institute of Astrophysics, Central China Normal University, Luoyu Road 152, Wuhan 433079, P.R. China

<sup>5</sup> ISDC Data Center for Astrophysics, Université de Genève, 16 chemin d'Écogia, 1290 Versoix, Switzerland

<sup>6</sup> School of Physics and Astronomy, Sun Yat-sen University, Zhuhai 519082, China

<sup>7</sup> National Astronomical Observatories, Chinese Academy of Sciences, A20 Datun Road, Beijing 100012, China

<sup>8</sup> School of Physics and Optoelectronic Engineering, Shandong University of Technology, Zibo 255000, China

October 1, 2024

## ABSTRACT

**Context.** In September 2022, the transient neutron star low-mass X-ray binary XTE J1701–462 went into a new outburst.

**Aims.** The objective of this work is to examine the evolution of the accretion geometry of XTE J1701–462 by studying the spectro-polarimetric properties along the Z track of this source. The simultaneous observations archived by the *Insight*-Hard X-ray Modulation Telescope (HXMT) and the Imaging X-ray Polarimetry Explorer (*IXPE*) give us the opportunity.

**Methods.** We present a comprehensive X-ray spectro-polarimetric analysis of XTE J1701–462, using simultaneous observations from *IXPE*, *Insight*-HXMT, and *NuSTAR*. For *IXPE* observations, two methods are employed to measure the polarization: a model-independent measurement with PCUBE and a model-dependent polarization-spectral analysis with XSPEC. The corresponding spectra from *Insight*-HXMT and *NuSTAR* are studied with two configurations that correspond to the eastern model and western model, respectively.

**Results.** Significant polarization characteristics are detected in XTE J1701–462. The polarization degree shows a decreasing trend along the Z track, reducing from  $(4.84 \pm 0.37)\%$  to  $(3.76 \pm 0.43)\%$  on the horizontal branch and jumping to  $\leq 1\%$  on the normal branch. The simultaneous spectral analysis from *Insight*-HXMT and *NuSTAR* suggests that the evolution of the PD is closely linked to changes in the flux of the Comptonized component and its covering factor along the Z track, supporting a shrinking corona.

**Conclusions.**

**Key words.** accretion, accretion disks – neutron stars – polarization – X-rays: binaries – X-rays: individual: XTE J1701–462

## 1. Introduction

Weakly magnetized neutron stars in low-mass X-ray binaries (NS-LMXBs) are believed to accrete mass via Roche-lobe overflow from a low mass stellar companion. These sources show intensity and spectral variations on time scales ranging from hours to months, and are historically divided into two classes, Z and atoll sources. The classification is based on the shape of their tracks in the X-ray hard-color/soft-color diagram (CCD), or their hard-color/intensity diagram (HID) (Hasinger & van der Klis 1989). The Z-sources trace out a ‘Z’-shaped track with three branches: horizontal branch (HB), normal branch (NB), and flaring branch (FB). The Z-sources are further classified into two sub-categories based on the shape and orientation of their branches. The Cyg-like Z-sources have prominent HB and weak FB, and vice-versa for the Sco-like Z-sources.

XTE J1701–462 is a NS-LMXB discovered with the All Sky Monitor (ASM) of the Rossi X-ray Timing Explorer (RXTE) in January 2006 (Remillard et al. 2006). Among the NS-LMXBs,

XTE J1701–462 can be regarded as a rather unique object, which is the first source that shows both Z-like and Atoll-like behavior during one single outburst (Homan et al. 2007; Lin et al. 2009; Homan et al. 2010). In the first 10 weeks of its outburst, XTE J1701–462 evolved from a Cyg-like into a Sco-like Z source, and during the decay, it showed an Atoll-like behavior (Homan et al. 2007; Lin et al. 2009; Bu et al. 2015). The orbital inclination of the system is lower than  $75^\circ$  (Lin et al. 2009). In September 2022, XTE J1701–462 experienced a new outburst, the second one since its discovery in 2006 (Iwakiri et al. 2022).

The X-ray emission of NS-LMXBs can be generally described by models that include a soft/thermal component, either a single-temperature blackbody emission from the NS surface or a multicolor blackbody emission from the accretion disk, and a hard/Comptonized component resulting from Comptonization of soft photons scattered by the hot electron plasma in the corona. Based on the choices of the thermal and Comptonized components, there are two classical models, the “eastern model” and the “western model”. In the “eastern model”, the thermal component is described by a multicolor disk, while the Comptonized com-

\* bu@astro.uni-tuebingen.de

ponent is described by a weakly Comptonized blackbody that may originate from the boundary layer (BL) between the disk and the NS (Pringle 1977; Shakura & Sunyaev 1988; Popham & Sunyaev 2001) or the spreading layer (SL) near the surface of the neutron star (Inogamov & Sunyaev 1999; Suleimanov & Poutanen 2006). In the “western model”, the thermal component is a single-temperature blackbody from the BL and the Comptonized emission is from the disk (White et al. 1988; Piraino et al. 2000, 2007; Di Salvo et al. 2000, 2001; Chen et al. 2012; Wang et al. 2019).

Because of the strong degeneracy found in the spectral models (Barret 2001), spectroscopy alone is usually insufficient to give a full picture of the accretion geometry. In addition to spectroscopy, both timing and polarization analysis can offer extra perspectives into its examination. For instance, the Fourier-frequency resolved spectroscopy analysis of a sample of atoll and Z sources has provided extra support for the eastern model, based on the observation that the Fourier-frequency resolved spectrum closely resembles the spreading layer spectrum at the frequencies of quasi-periodic oscillations (Gilfanov et al. 2003; Revnivtsev & Gilfanov 2006; Revnivtsev et al. 2013). Besides, X-ray polarimetry offers a unique perspective to the geometry of the system, while eliminating the degeneracy left by spectroscopy. In particular, Compton scattering yields a polarization signal that is highly sensitive to the geometry of the scattering material (Gnarini et al. 2022; Capitanio et al. 2023). Various geometries and viewing angles will result in markedly different polarization degrees (PDs) and polarization angles (PAs).

The Imaging X-ray Polarimetry Explorer (*IXPE*) operates in the 2–8 keV band providing a unique opportunity to investigate the accretion geometric evolution through X-ray polarimetry and constraining the coronal geometry of NS-LMXBs. To date, *IXPE* has targeted a variety of NS-LMXBs, including the Z-sources Cyg X–2 (Farinelli et al. 2023) and GX 5–1 (Fabiani et al. 2024), the Z-atoll transient source XTE J1701–462 (Jayasurya et al. 2023; Cocchi et al. 2023), and two atoll sources, GS 1826–238 (Capitanio et al. 2023) and GX 9+9 (Chatterjee et al. 2023; Ursini et al. 2023).

In this work, we conduct a spectro-polarimetric analysis of the NS-LMXB XTE J1701–462, using observations from *IXPE*, *NuSTAR* and *Insight-HXMT*. The paper is structured as follows. In Section 2, we describe the observations and data reduction. In Section 3, we report on the analysis of the spectral and polarimetric data. Section 4 is devoted to the discussion of the results. Finally, we summarize our conclusions in Section 5.

## 2. OBSERVATIONS AND DATA REDUCTION

### 2.1. *IXPE*

*IXPE* observed the NS-LMXB XTE J1701–462 in 2022 September 29–30 (Epoch1) and 2022 October 8–9 (Epoch2) with net exposure times of 46.2 ks and 46.4 ks, respectively. We analyze the *IXPE* data using both the Python-based software *IXPEobssim* v30.2.21 (Baldini et al. 2022) and *XSPEC*. The source region is defined as a circular area with a radius of 60″, while the background region is defined as an annular area with an inner radius of 180″ and an outer radius of 240″.

The polarization parameters (PD and PA) are extracted in the energy band 2–8 keV using the model-independent PCUBE algorithm of *XPBIN* tool (Kislat et al. 2015). We also perform a spectro-polarimetric model-dependent fit of the data using *XSPEC*. Source and background spectra corresponding to the Stokes parameters I, Q, and U for all DUs are extracted using

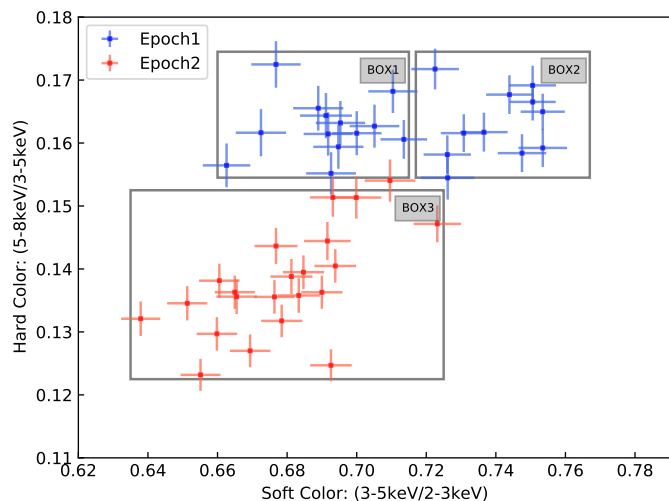


**Fig. 1.** *IXPE* colour–colour diagram of XTE J1701–462. The hard colour and soft colour are defined as the count rate ratios 5–8 keV/3–5 keV and 3–5 keV/2–3 keV, respectively. The blue points correspond to Epoch1 on the HB, while the orange points correspond to Epoch2 on the NB.

XSELECT. The latest *IXPE* response matrices (v12) are used in spectral fitting.

### 2.2. *Insight-HXMT*

*Insight-HXMT* observed the source from 2022 September 7 to October 2, which fully overlaps with the Epoch1 of *IXPE* observations. There are three telescopes onboard *Insight-HXMT*: the high-energy X-ray telescope (HE: 20–250 keV; Liu et al. 2020), the medium-energy X-ray telescope (ME: 5–30 keV; Cao et al. 2020), and the low-energy X-ray telescope (LE: 1–15 keV; Chen et al. 2020).

The data are processed using the *hpipeline* under *Insight-HXMT* Data Analysis Software (HXMTDAS) version 2.05. The data are filtered using the criteria recommended by the *Insight-HXMT* team: a pointing offset angle smaller than 0.04°; an elevation angle greater than 10°; a geomagnetic cutoff rigidity value larger than 8; and data usage at least 300 s before and after the South Atlantic Anomaly (SAA) passage. To avoid potential contamination from bright earth and nearby sources, only the small field of view (FoVs) were applied. Given that the spectrum above 30 keV is dominated by the background for this source, we further select the 2–30 keV energy range for our spectral fitting.

### 2.3. *NuSTAR*

Since *Insight-HXMT* lacks the simultaneous observation of Epoch2, we include *NuSTAR* observation for spectral analysis. *NuSTAR* observed the source on 2022 October 8 (ObsID 90801325002), with a net exposure of 12.2 ks, which overlaps with Epoch2 of *IXPE*. We process the *NuSTAR* data using v.1.9.7 of the *NuSTARDAS* pipeline with the latest CALDB files. The spectra are extracted from a circular region of the radius 60″ centered on the source location. The background is estimated from a blank region on the detector furthest from source location to avoid source photons. The spectra and light curves are extracted using the *nuproduct* task. We re-bin the spectra with 50 counts per bin by using the *ftgrouppha* task. Similar to *Insight-HXMT*, the selected energy range is 3–30 keV.

**Table 1.** Polarimetric parameters measured with PCUBE and XSPEC, respectively. The polarization-spectral fitting was performed using model: `tbabs*polconst(diskbb+thcomp*bbodyrad+gaussian)`. The uncertainties are given at  $1\sigma$  confidence level.

PCUBE			
Parameter	BOX1	BOX2	BOX3
Location	HB	HB	NB
PD (%)	$4.98 \pm 0.44$	$3.79 \pm 0.54$	$0.9 \pm 0.3$
PA ( $^\circ$ )	$139.72 \pm 2.58$	$149.20 \pm 4.29$	$130.0 \pm 13.6$
XSPEC			
Parameter	BOX1	BOX2	BOX3
Location	HB	HB	NB
PD (%)	$5.07 \pm 0.32$	$3.72 \pm 0.35$	$0.8 \pm 0.3$
PA ( $^\circ$ )	$136.42 \pm 3.44$	$152.31 \pm 2.43$	$135.3 \pm 12.6$

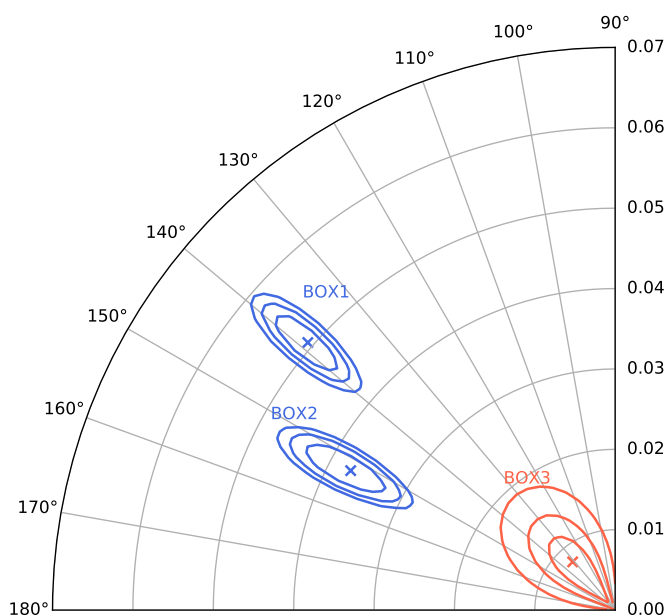


**Fig. 2.** Contour plot of PD and PA at 68.27, 95.45, and 99.73 percent confidence levels in the 2–8 keV band obtained with XSPEC. The polarization-spectral fitting was performed using model: `tbabs*polconst(diskbb+thcomp*bbodyrad+gaussian)`. The parameters are shown in Table 3

### 3. Results

#### 3.1. Polarimetric Analysis

The CCD of the source for the *IXPE* observations is shown in Fig. 1. We define the soft color as the ratio of count rates in the 3–5 keV to the 2–3 keV bands, and the hard color as the ratio of count rates in the 5–8 keV to the 3–5 keV energy bands. During Epoch1, the source is observed on the HB. Epoch2, the source moves to the NB (Jayasurya et al. 2023; Cocchi et al. 2023).

Polarization measured from the model-independent method PCUBE, gives a significant PD of  $4.5 \pm 0.3\%$  and a PA of  $143.5 \pm 2.3^\circ$  for HB, while a much weaker PD of  $0.9 \pm 0.3\%$  for NB which is less than the minimum detectable polarization (MDP) at the 99% confidence level. These results are in agreement with those reported by Jayasurya et al. (2023) and Cocchi et al. (2023).

To investigate the evolution of the polarization characteristics along the Z-track, we further divide Epoch1 into two segments, BOX1 and BOX2, and study their polarization characteristics separately. The total exposure time of BOX1 and BOX2 is approximately equal. Given that the PD for Epoch2 is below the minimum detectable limit, we keep the original selection for it and define it as BOX3. Due to the low statistics, further study on the energy-dependent polarization of BOX1 and BOX2 is not possible.

We first use the PCUBE method to measure the PD and PA of the three boxes. For BOX1 and BOX2, the PDs are  $4.98 \pm 0.44\%$  and  $3.79 \pm 0.54\%$ , with corresponding PAs of  $139.72 \pm 2.58^\circ$  and  $149.20 \pm 4.29^\circ$ , respectively. The results are listed in Table 2. The results show that as the source evolves through HB, the PD decreases and the PA increases, and when the source evolves to the NB, both PD and PA decrease.

We further cross-check the results by fitting the Stokes I, Q, and U spectra with XSPEC. We apply the model `tbabs*polconst(diskbb+thcomp*bbodyrad)` for the broadband spectral analysis. In this model, the `polconst` component carries the polarimetric information, assuming a constant PD and PA across the entire spectrum. The `thComp` component describes the Comptonized emission from hot electron plasma, while the `diskbb` component represents emission from a standard accretion disc. Limited by the statistics and energy band of the *IXPE*, the parameters are fixed to the values that are given from the spectral fitting of the *Insight-HXMT* observation (see Sec. 3.2 for more details), leaving only the normalization and polarization parameters to vary freely.

The PD and PA obtained from the polarization-spectral fitting are listed in Table 2. These polarization parameters are in great agreement with the results given by the PCUBE method. Fig. 2 shows the two-dimensional contour plots for PD and PA. We also attempted to measure the polarization information of individual spectral components, but due to the low statistics of the data in each box, it was not possible to constrain the polarization information for each component.

#### 3.2. Spectral properties

We perform detailed spectral fitting on the three boxes using the data from *Insight-HXMT* and *NuSTAR*. A Comptonized component (`thcomp`; Zdziarski et al. 2020) plus either a multi-color disk blackbody (`diskbb`; hereafter Model 1) or a single temper-

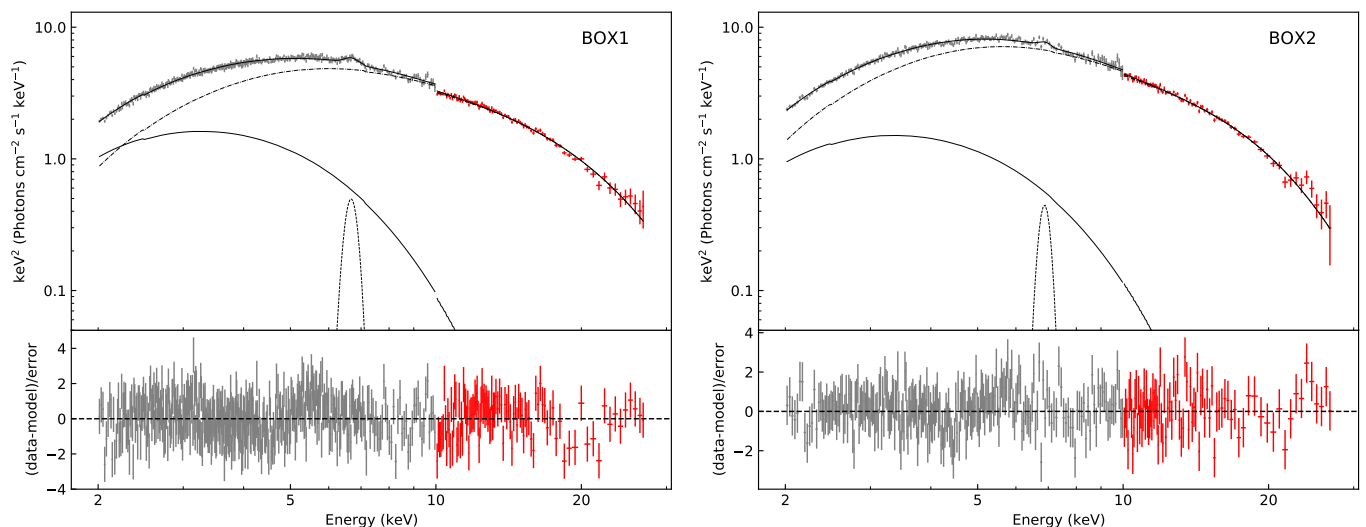


**Fig. 3.** *Insight-HXMT* spectrum fitted with Model 1. The gray and red points represent LE and ME, respectively. The full model is shown in thick-solid line, the thermal emission `diskbb` is shown in dashed line, and the Comptonization component `thcomp` is shown in dot-dashed line.

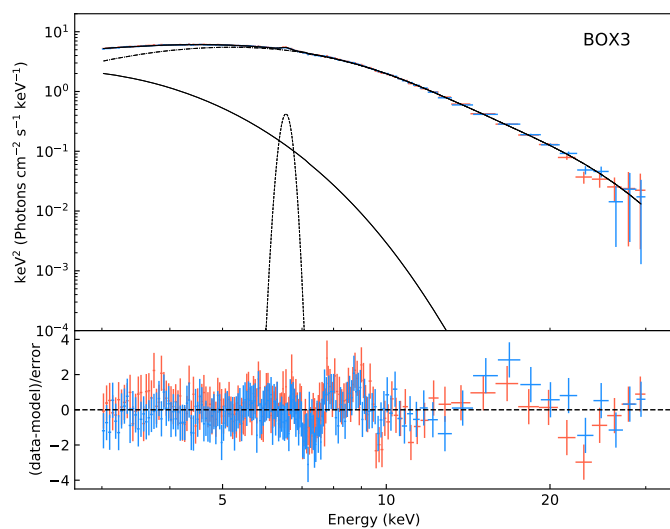


**Fig. 4.** *NuSTAR* spectrum fitted with Model 1. The blue and orange points represent FPMA and FPMB, respectively. The full model is shown in thick-solid line, the thermal emission `diskbb` is shown in dashed line, and the Comptonization component `thcomp` is shown in dot-dashed line.

ature blackbody (`bbodyrad`; hereafter Model 2) are applied to fit the 2–30 keV spectra. For all the spectra, a neutral Galactic absorption component, modeled with `TBabs` is added (Wilms et al. 2000). We adopt the abundances in Wilms et al. (2000) as appropriate for absorption by the Galactic interstellar medium and adopt the recommended cross-sections of Verner et al. (1996).

In Model 1, the seed photons for Comptonization are assumed to follow a blackbody distribution, with the thermal emission originating from the accretion disk, which is known as the “eastern model”. This model typically assumes a shell-like corona surrounding the neutron star, as most of the seed photons from the neutron star get scattered and Comptonized by the hot corona, while almost the entire disc can be directly observed. In Model 2, the seed photons are assumed to follow a multi-temperature disk blackbody distribution, with the thermal emission originating from the boundary layer, which is known as the

“western model”. The slab-like corona can be considered representative of the western model because most of the disc photons are scattered by the corona, while the NS radiation can be directly detected.

It is important to note that the `thcomp` model itself does not inherently allow for switching between shell-like and slab-like configurations of the Comptonization region. Instead, these geometrical interpretations are based on the assumptions made about the origin of the seed photons and the thermal component in the context of the applied models.

Both models give acceptable fits to the spectra. The best-fitting values are given in Table 2 and Table 3. The spectra and residuals for Model 1 are shown in Fig. 3 and Fig. 4. We further calculate the photon flux ratios for thermal and Comptonized emission, separately. The spectral fitting results show that, as the source evolves from BOX1 to BOX3 along the Z track, the contribution from the Comptonized emission in Model 1 slightly increases, with the flux ratio increasing from 71% to 84%. On the contrary, in Model 2, the contribution of the Comptonized emission gives an opposite trend, with the flux ratio decreasing from 65% to 21%.

In addition to the photon flux, the covering fraction of the Comptonization medium relative to the input seed photons, denoted as  $f$ , also demonstrates significant evolution. For Model 1,  $f$  decreases from 0.7 to 0.39 in the HB and approaches zero in the NB. For Model 2,  $f$  remains close to 1 in the HB and similarly drops to near zero in the NB. Given that  $f$  approaches zero in the NB for both models, the spectral model in the NB can be approximated as a combination of `bbodyrad` and `diskbb`. Similar findings have also been observed in the Z source GX 5–1. Fabiani et al. (2024) reported that in GX 5–1,  $f$  is approximately 1 in the HB and near zero in the NB/FB, with the PD in the HB being higher than in the NB/FB.

## 4. Discussion

In this paper, we present a comprehensive X-ray spectropolarimetric analysis on NS-LMXB XTE J1701–462, using simultaneous observations from *IXPE*, *Insight-HXMT*, and *NuSTAR* for the 2022 outburst. During the observations, the source evolves from the HB (Epoch1) to the NB (Epoch2), tracing a Z

**Table 2.** The best-fitting spectral parameters of Model 1. The data of BOX1 and BOX2 are from *Insight*-HXMT, while BOX3 is from *NuSTAR*. Uncertainties are given at 90% confidence level for one parameter of interest.

Model 1 : tbabs*(diskbb+thcomp*bbbodyrad+gaussian)			
Parameters	BOX1	BOX2	BOX3
tbabs			
$N_{\text{H}}$ ( $10^{22}\text{cm}^{-2}$ )		1.96*	
diskbb			
$kT_{\text{in}}$ (keV)	$1.13^{+0.05}_{-0.06}$	$1.17^{+0.06}_{-0.06}$	$0.71^{+0.02}_{-0.02}$
norm	$180^{+27}_{-20}$	$146^{+6}_{-5}$	$2443^{+191}_{-208}$
thComp			
$\Gamma$	$2.16^{+0.09}_{-0.04}$	$1.68^{+0.13}_{-0.14}$	$1.18^{+0.05}_{-0.03}$
$kT_{\text{e}}$ (keV)	$3.53^{+0.19}_{-0.07}$	$2.91^{+0.05}_{-0.04}$	$2.52^{+0.05}_{-0.05}$
$f$	$0.70^{+0.05}_{-0.02}$	$0.39^{+0.04}_{-0.04}$	$0.04^{+0.01}_{-0.01}$
bbbodyrad			
$kT_{\text{bb}}$ (keV)	$1.15^{+0.02}_{-0.01}$	$1.18^{+0.04}_{-0.03}$	$1.25^{+0.01}_{-0.01}$
norm	$540^{+27}_{-48}$	$729^{+29}_{-43}$	$474^{+15}_{-15}$
gaussian			
LineE	$6.66^{+0.08}_{-0.03}$	$6.86^{+0.02}_{-0.01}$	$6.53^{+0.04}_{-0.02}$
$\sigma$	$0.20^{+0.02}_{-0.05}$	$0.18^{+0.08}_{-0.09}$	$0.13^{+0.05}_{-0.08}$
norm ( $10^{-3}$ )	$5.81^{+0.61}_{-1.63}$	$4.46^{+1.24}_{-1.34}$	$3.28^{+0.58}_{-0.59}$
2–8 keV flux ratios			
$F_{\text{dikbb}}/F_{\text{tot}}$	22%	17%	12%
$F_{\text{thcomp}}/F_{\text{tot}}$	78%	83%	88%
2–8 keV photon flux ratios			
$F_{\text{diskbb}}/F_{\text{tot}}$	29%	24%	16%
$F_{\text{thcomp}}/F_{\text{tot}}$	71%	76%	84%
$\chi^2/\text{d.o.f.}$	1216/1233	1201/1233	1331/1348

track on the CCD. This work is focused on investigating the evolution of correlated polarimetric and spectral properties along the Z track in XTE J1701–462. In particular, the broadband energy spectra from *Insight*-HXMT and *NuSTAR* allow us to establish more precise constraints on the spectral parameters.

Significant polarization is detected on the HB and only a very weak polarization is detected on the NB. The PD is found to decrease from  $\sim 5\%$  to  $\sim 3.8\%$  along the HB in 2–8 keV, from BOX1 to BOX2, and drop to  $\leq 1\%$  on the NB (BOX3), while the corresponding PA increases along the HB and then decreases on the NB. The high polarization degree detected on the HB of XTE J1701–462 in 2–8 keV excludes the possibility of the accretion disk being the source of the polarized radiation since the disk emission dominates below 3 keV and the PD measured from the disk is less than 1.6% in this source (Cocchi et al. 2023). According to the polarization measurements by Jayasurya et al. (2023), the increase in PD with energy further contradicts the hypothesis that the polarization primarily originates from the accretion disk.

In principle, a reflection component from the ionized inner accretion disk can produce a PD of 6% in the total spectrum

**Table 3.** The best-fitting spectral parameters of Model 2. The data of BOX1 and BOX2 are from *Insight*-HXMT, while BOX3 is from *NuSTAR*. Uncertainties are given at 90% confidence level for one parameter of interest.

Model 2 : tbabs*(bbbodyrad+thcomp*diskbb+gaussian)			
Parameters	BOX1	BOX2	BOX3
tbabs			
$N_{\text{H}}$ ( $10^{22}\text{cm}^{-2}$ )		1.50*	
bbbodyrad			
$kT_{\text{bb}}$ (keV)	$1.03^{+0.01}_{-0.01}$	$1.12^{+0.01}_{-0.01}$	$1.25^{+0.01}_{-0.01}$
norm	$426^{+13}_{-17}$	$613^{+8}_{-12}$	$445^{+14}_{-13}$
thComp			
$\Gamma$	$3.10^{+0.12}_{-0.28}$	$2.81^{+0.24}_{-0.13}$	$1.27^{+0.18}_{-0.13}$
$kT_{\text{e}}$ (keV)	$5.06^{+0.39}_{-0.57}$	$3.42^{+0.31}_{-0.27}$	$2.53^{+0.10}_{-0.06}$
$f$	$1.00^{+0.00}_{-0.05}$	$1.00^{+0.10}_{-0.06}$	$0.08^{+0.03}_{-0.01}$
diskbb			
$kT_{\text{in}}$ (keV)	$2.26^{+0.06}_{-0.07}$	$2.61^{+0.02}_{-0.02}$	$0.71^{+0.01}_{-0.02}$
norm	$18^{+2}_{-2}$	$10^{+2}_{-1}$	$2073^{+173}_{-209}$
gaussian			
LineE	$6.65^{+0.07}_{-0.07}$	$6.86^{+0.10}_{-0.06}$	$6.53^{+0.04}_{-0.02}$
$\sigma$	$0.22^{+0.02}_{-0.02}$	$0.19^{+0.04}_{-0.01}$	$0.13^{+0.03}_{-0.08}$
norm ( $10^{-3}$ )	$6.39^{+0.58}_{-0.69}$	$4.89^{+0.14}_{-0.68}$	$3.45^{+0.24}_{-0.53}$
2–8 keV flux ratios			
$F_{\text{bbbodyrad}}/F_{\text{tot}}$	32%	48%	80%
$F_{\text{thcomp}}/F_{\text{tot}}$	68%	52%	20%
2–8 keV photon flux ratios			
$F_{\text{bbbodyrad}}/F_{\text{tot}}$	35%	58%	79%
$F_{\text{thcomp}}/F_{\text{tot}}$	65%	42%	21%
$\chi^2/\text{d.o.f.}$	1223/1233	1133/1233	1332/1348

(Lapidus & Sunyaev 1985). However, in this case, there are no significant reflection features observed in the spectra. Our spectral fitting results indicate that, apart from the broad iron line, no additional reflection components are required to fit the spectrum, suggesting that the contribution of the reflection component to the polarization can be neglected.

Seed photons can become polarized after the inverse Compton scattering in the corona, which is considered one of the main sources of photon polarization (Poutanen & Svensson 1996). In this scenario, the polarization degree highly depends on the geometrical configurations of accretion flow and the spectral states of the source. Specifically, for a slab-like corona, the up-scattered seed photons mainly come from the accretion disk, while for a shell-like corona, the up-scattered seed photons mainly come from the surface of the neutron star.

Based on these scenarios, we performed spectral fitting on data from *Insight*-HXMT and *NuSTAR*. The two models used for spectral fitting correspond to different sources of seed photons under varying geometrical configurations of the corona. Simultaneous spectral analysis in the 2–30 keV range reveals a

significant redistribution between the thermal and Comptonized components along the Z track, as well as a notable evolution in the covering factor of the Comptonized component.

The results from Model 1 indicate that from BOX1 to BOX3, the flux of the Comptonized component gradually increases. If the polarization originates from inverse Compton scattering in the corona, we would generally expect an increasing PD. However, the observed PD actually decreases during this process. This discrepancy is likely due to the dilution of the Comptonized flux caused by a decreasing covering factor. The observed covering factor shows a decreasing trend consistent with the PD from BOX1 to BOX3. Under the eastern model assumption, this might suggest that as the source evolves along the Z track from the HB to the NB, there is a reduction in the corona's thickness/size or the coverage of the boundary layer on the neutron star's surface, leading to a reduction in PD.

According to the results from Model 2, the flux of the Comptonized component exhibits an opposite trend compared to Model 1, decreasing by 44% from BOX1 to BOX3. Previous studies using Rossi-XTE observations on XTE J1701–462 have also suggested that the Comptonized emission decreases at a roughly constant accretion rate along the HB (Lin et al. 2009; Li et al. 2014). Correspondingly, the covering factor remains close to 1 on the HB and approaches 0 on the NB. With a constant covering factor, the decrease in the Comptonized flux from BOX1 to BOX2 can naturally explain the reduction in PD. In BOX3, a scenario similar to Model 1 occurs, where the near-zero covering factor results in a lack of polarized Comptonized photons. Under the Western model hypothesis, this might indicate that an extended slab/wedge corona covered most of the inner disk and gradually thinned as the source evolved along the Z track, resulting in a decrease in PD.

It is noteworthy that in both scenarios, the extremely low PD and near-zero covering factor of the Comptonized component on the NB indicate a significant evolution in the accretion flow from the HB to the NB, with the Comptonized corona nearly disappearing in this process. The co-evolution of polarization and the Comptonized component flux further corroborates the Comptonized origin of the observed polarization in XTE J1701–462.

## 5. Summary

In this study, we present an in-depth analysis of the spectropolarimetric evolution along the Z track of the NS-LMXB XTE J1701–462. Our findings reveal that the PD exhibits a monotonically decreasing trend from the HB to NB. The combined results from spectral and polarimetric measurements align with the scenario of a shrinking corona.

*Acknowledgements.* This work made use of the data from the *Insight-HXMT* mission, a project funded by the China National Space Administration (CNSA) and the Chinese Academy of Sciences (CAS), and data and/or software provided by the High Energy Astrophysics Science Archive Research Center (HEASARC), a service of the Astrophysics Science Division at NASA/GSFC. This work is supported by the National Key RD Program of China (2021YFA0718500) and the National Natural Science Foundation of China (NSFC) under grant Nos. U1838202, 12273030, 11733009, 11673023, U1938102, U2038104, U2031205, 12233002, 12133007, 12333007, the CAS Pioneer Hundred Talent Program (grant No. Y8291130K2) and the Scientific and Technological Innovation Project of IHEP (grant No. Y7515570U1). This work was partially supported by the International Partnership Program of the CAS (grant No. 113111KYSB20190020).

## References

- Baldini, L., Bucciantini, N., Lalla, N. D., et al. 2022, *SoftwareX*, 19, 101194  
 Barret, D. 2001, *Advances in Space Research*, 28, 307  
 Bu, Q., Chen, L., Li, Z.-s., et al. 2015, *The Astrophysical Journal*, 799, 2  
 Cao, X., Jiang, W., Meng, B., et al. 2020, *Science China Physics, Mechanics, and Astronomy*, 63, 249504  
 Capitanio, F., Fabiani, S., Gnarini, A., et al. 2023, *ApJ*, 943, 129  
 Chatterjee, R., Agrawal, V. K., Jayasurya, K. M., & Katoch, T. 2023, *MNRAS*, 521, L74  
 Chen, Y., Cui, W., Li, W., et al. 2020, *Science China Physics, Mechanics, and Astronomy*, 63, 249505  
 Chen, Y.-P., Zhang, S., Zhang, S.-N., Li, J., & Wang, J.-M. 2012, *ApJ*, 752, L34  
 Cocchi, M., Gnarini, A., Fabiani, S., et al. 2023, *A&A*, 674, L10  
 Di Salvo, T., Robba, N. R., Iaria, R., et al. 2001, *ApJ*, 554, 49  
 Di Salvo, T., Stella, L., Robba, N. R., et al. 2000, *ApJ*, 544, L119  
 Fabiani, S., Capitanio, F., Iaria, R., et al. 2024, *A&A*, 684, A137  
 Farinelli, R., Fabiani, S., Poutanen, J., et al. 2023, *MNRAS*, 519, 3681  
 Gilfanov, M., Revnivtsev, M., & Molkov, S. 2003, *A&A*, 410, 217  
 Gnarini, A., Ursini, F., Matt, G., et al. 2022, *MNRAS*, 514, 2561  
 Hasinger, G. & van der Klis, M. 1989, *A&A*, 225, 79  
 Homan, J., van der Klis, M., Fridriksson, J. K., et al. 2010, *ApJ*, 719, 201  
 Homan, J., van der Klis, M., Wijnands, R., et al. 2007, *ApJ*, 656, 420  
 Inogamov, N. A. & Sunyaev, R. A. 1999, *Astronomy Letters*, 25, 269  
 Iwakiri, W., Serino, M., Negoro, H., et al. 2022, *The Astronomer's Telegram*, 15592, 1  
 Jayasurya, K. M., Agrawal, V. K., & Chatterjee, R. 2023, *MNRAS*, 525, 4657  
 Kislat, F., Clark, B., Beilicke, M., & Krawczynski, H. 2015, *Astroparticle Physics*, 68, 45  
 Lapidus, I. I. & Sunyaev, R. A. 1985, *MNRAS*, 217, 291  
 Li, Z., Chen, L., Qu, J., et al. 2014, *Astrophys. J.*, 786, 119  
 Lin, D., Remillard, R. A., & Homan, J. 2009, *ApJ*, 696, 1257  
 Liu, C., Zhang, Y., Li, X., et al. 2020, *Science China Physics, Mechanics, and Astronomy*, 63, 249503  
 Piraino, S., Santangelo, A., di Salvo, T., et al. 2007, *A&A*, 471, L17  
 Piraino, S., Santangelo, A., & Kaaret, P. 2000, *A&A*, 360, L35  
 Popham, R. & Sunyaev, R. 2001, *ApJ*, 547, 355  
 Poutanen, J. & Svensson, R. 1996, *ApJ*, 470, 249  
 Pringle, J. E. 1977, *MNRAS*, 178, 195  
 Remillard, R. A., Lin, D., ASM Team at MIT, & NASA/GSFC. 2006, *The Astronomer's Telegram*, 696, 1  
 Revnivtsev, M. G. & Gilfanov, M. R. 2006, *A&A*, 453, 253  
 Revnivtsev, M. G., Suleimanov, V. F., & Poutanen, J. 2013, *MNRAS*, 434, 2355  
 Shakura, N. I. & Sunyaev, R. A. 1988, *Advances in Space Research*, 8, 135  
 Suleimanov, V. & Poutanen, J. 2006, *MNRAS*, 369, 2036  
 Ursini, F., Farinelli, R., Gnarini, A., et al. 2023, *A&A*, 676, A20  
 Verner, D. A., Ferland, G. J., Korista, K. T., & Yakovlev, D. G. 1996, *ApJ*, 465, 487  
 Wang, Y., Méndez, M., Altamirano, D., et al. 2019, *MNRAS*, 484, 3004  
 White, N. E., Stella, L., & Parmar, A. N. 1988, *ApJ*, 324, 363  
 Wilms, J., Allen, A., & McCray, R. 2000, *ApJ*, 542, 914  
 Zdziarski, A. A., Szanecki, M., Poutanen, J., Gierliński, M., & Biernacki, P. 2020, *MNRAS*, 492, 5234